

The energy distribution, angular distribution, and alignment of the $O(^1D_2)$ fragment from the photodissociation of ozone between 235 and 305 nm

Scott M. Dylewski

Department of Applied and Engineering Physics, Cornell University, Ithaca, New York 14853

Joseph D. Geiser and Paul L. Houston

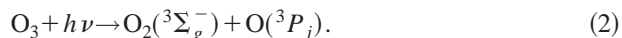
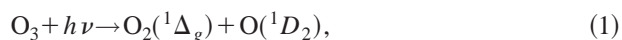
Department of Chemistry and Chemical Biology, Cornell University, Ithaca, New York 14853

(Received 3 July 2001; accepted 3 August 2001)

Resonance-enhanced multiphoton ionization and time-of-flight product imaging have been used to study the $O_3(\tilde{X}^1A_1) + h\nu \rightarrow O(^1D_2) + O_2(^1\Delta_g)$ channel of the UV photodissociation of ozone at 235, 245, 255, 265, 275, 285, 298, and 305 nm. At all wavelengths, the vibrational populations, the spatial anisotropy parameter β , and the $O(^1D_2)|m_j|$ populations were determined. The corresponding vibrational populations of $O_2(^1\Delta_g)$ were peaked at $v=0$. The spatial anisotropy parameter was determined for each vibrational level and changed monotonically from about 1.2 at 235 nm to 1.7 at 298 nm. At all wavelengths, $|m_j|$ populations were peaked at $|m_j|=0$. A full density matrix method was used to determine the $a_q^{(2)}(p)$ parameters at 255 and 298 nm, where most of the signal was found to be from parallel, incoherent excitation. The data support a dissociation mechanism in which excitation occurs to a state of A' symmetry and there is substantial bending of the ozone before dissociation. © 2001 American Institute of Physics. [DOI: 10.1063/1.1405439]

I. INTRODUCTION

In the Hartley band, ozone primarily dissociates through the spin conserved channels,



Most (about 90%) of the dissociating ozone molecules will follow channel (1), while about 10% follow channel (2). Many studies have measured the energy distributions of the fragments for each channel.¹⁻⁸ Results from these researchers have concluded that between ~ 220 nm and the threshold at 310 nm, the $O_2(^1\Delta_g)$ fragment from the photodissociation of ozone contains population in each energetically accessible vibrational level. Most population resides in the ground vibrational level, and all levels have a high degree of rotational excitation. These results are consistent with a rotationally impulsive but vibrationally adiabatic dissociation mechanism.⁶ A full understanding of the photodissociation process includes not only knowledge of the energy partitioning between the photofragments but also the geometry of the molecule as it dissociates and even the relative orientation of any angular momentum vectors in the departing fragments.

When a molecule is dissociated with linearly polarized light, the photofragment spatial distribution follows the well-known equation,

$$I(\theta) = (1/4\pi)[1 + \beta P_2(\cos \theta)], \quad (3)$$

where θ is the angle between the photolysis laser polarization and the fragment velocity vector, and β is the spatial anisotropy parameter. If the molecule dissociates quickly relative to its rotational lifetime, then β is given by the simple equation

$$\beta = 2P_2(\cos \chi), \quad (4)$$

where χ is the angle in the molecular frame between the transition dipole moment and the velocity vector of the fragment. Thus for rapid dissociations, a measurement of the spatial anisotropy parameter enables a determination of the geometry of the molecule at the time of dissociation if the direction of the transition dipole moment is known. For dissociation of ozone this transition dipole moment lies in the plane of the molecule and perpendicular to the C_{2v} axis.⁹ If the excited state of ozone (which dissociates in a fraction of a picosecond after absorption of a photon¹⁰⁻¹²) were to dissociate from the same geometry as the ground state, where the O-O-O angle is 116.8°, then the photofragment angular distribution would be described by $\beta=1.18$. Many of the energy distribution studies mentioned above have also measured the spatial anisotropy parameter of $O(^1D)$ from ozone in the Hartley band.^{1,3-5,8} Measurements performed near the 250 nm peak of the Hartley band using rotationally cold ozone molecules have shown that the excited state geometry is very close to the ground state geometry.⁹ However, at longer wavelengths near 285 nm, the spatial anisotropy parameter is larger, indicating dissociation from a larger bond angle.

Vector correlations in photodissociation dynamics can also provide insight into the reaction dynamics.¹³ For example, previous researchers in this laboratory⁸ photodissociated ozone at 248 nm and used 2+1 resonance-enhanced multiphoton ionization (REMPI) to probe the $O_2(^1\Delta_g)$ fragment from reaction (1). Different REMPI laser polarizations were used to illustrate a correlation between the velocity, \mathbf{v} , of the $O_2(^1\Delta_g)$ fragment and its angular momentum, \mathbf{J} . Since $O_2(^1\Delta_g)$ from reaction (1) was known to be formed in high

rotational levels, these authors used a semiclassical approximation to model the reaction dynamics. In the past, most such vector correlation studies have relied on semiclassical approximations of full quantum-mechanical theories, an approach that was justified by the high rotational states being probed. When detecting an atomic fragment such as $O(^1D)$, it is not possible to use a semiclassical approximation for the angular momentum vector. Recent theoretical work has provided a method to extract the diagonal^{14,15} or full^{16–20} angular momentum density matrix for such atomic fragments. Determination of the density matrix allows for the determination of the shape of the electron cloud of the atomic fragment, i.e., the alignment of the atomic orbitals.

In the case of ozone, the molecule indeed dissociates to produce an anisotropic angular distribution as well as a speed distribution of fragments. During the dissociation process, the atomic orbital angular momentum may be preferentially aligned or “polarized” relative to its recoil velocity; one example would be $\mathbf{J} \perp \mathbf{v}$. The $\mathbf{v}-\mathbf{J}$ correlation is reflected in a measurement of the m_j populations, where m_j is the projection of the angular momentum along the relative velocity vector of the dissociation fragments. Since the 2 + 1 REMPI detection method with linearly polarized light is sensitive to the alignment of \mathbf{J} , the probability of ionizing fragments depends upon the recoil angle. By measuring the photofragment angular dependence and comparing it with theoretical models, we can extract the speed distribution, the spatial anisotropy parameter β , and the molecular frame $|m_j|$ populations of the $O(^1D)$ fragment from the photodissociation of ozone.

Despite several recent theoretical treatments,^{14,15,17–23} there have been few measurements of the complete angular momentum density matrix of an atomic fragment from a photodissociation. The initial theory and experiments were limited to finding the diagonal elements of the density matrix, i.e., the m_j populations (equivalent to limiting the spherical tensor expansion to only $q=0$ in the molecular frame). Since two-photon probes were frequently used, measurements were limited in many cases to determining the $|m_j|$ populations or $A_{|q|}^{(k)}$. Early imaging experiments simply hinted at the existence of higher-order terms in the angular distribution because it did not fit a simple $1 + \beta P_2(\cos \theta)$ shape.^{24,25} Later, product imaging was used to measure the $|m_j|$ populations of $S(^1D_2)$ from OCS (Ref. 15) and $O(^1D_2)$ from N_2O .²⁶ More recently, experiments which incorporate the full density matrix method have been able to measure coherence effects in the alignment of Cl from Cl_2 ,^{17,23,27} the orientation and alignment of Cl from ICl ,^{20,27} the alignment of $O(^3P_j)$ from NO_2 ,²⁸ the alignment of $O(^1D_2)$ from N_2O ,²⁹ and the orientation of $S(^1D_2)$ from OCS.³⁰

In this experiment, we have studied the $O_3(\tilde{X}^1A_1) + h\nu \rightarrow O(^1D_2) + O_2(^1\Delta_g)$ channel of the UV photodissociation of ozone at 235, 245, 255, 265, 275, 285, 298, and 305 nm. We measured the vibrational populations at all wavelengths, and for each vibrational level we determined the spatial anisotropy parameter, β , and the $|m_j|$ populations. A full density matrix method was used to determine the $a_q^{(2)}(p)$ alignment parameters at 255 and 298 nm.

II. EXPERIMENT

The technique of ion imaging has been described more fully elsewhere.^{31–33} A molecular beam of ozone was formed by flowing helium at about 810 Torr over ozone trapped on silica gel at -78°C . The resulting mixture of less than 1% ozone was expanded through a pulsed, 250 μm diam nozzle and collimated by a 500 μm diam skimmer mounted about 5 mm away from the nozzle. Two counterpropagating laser beams intersect the molecular beam at right angles. One laser dissociates the ozone molecules, and the other ionizes the resulting $O(^1D)$ fragments using the 2 + 1 REMPI processes at 203.7 or 205.4 nm.^{34,35} Due to the speed of the oxygen fragments with respect to the laser beam propagation direction, it was necessary to scan the ionization laser wavelength over the Doppler absorption profile to ensure equal detection of all the fragments.

The dissociation laser light between 230 and 305 nm was produced by frequency doubling the output of an optical parametric oscillator (Spectra-Physics MOPO-730) pumped by an injection-seeded Nd:YAG laser (Spectra-Physics GCR-230). Typical powers were 1–3 mJ/pulse with a pulse width of 9 ns. The output polarization was rotated, if necessary, with a double Fresnel rhomb, and then cleaned up with a stack of fused silica plates held at Brewster’s angle. The resultant polarization ratio was about 10:1. The light used to ionize the $O(^1D)$ fragments at 203 and 205 nm was generated by doubling the output of a Nd:YAG (Spectra-Physics GCR-230) pumped dye laser (Quanta Ray PDL1 with SR640 dye) in a KDP crystal, and then summing the fundamental with this doubled light in BBO. Typical powers achieved were 1 mJ/pulse with a pulsewidth of 9 ns. The polarization of the probe laser was rotated, if necessary, with a double Fresnel rhomb. The resultant polarization ratio was 10:1. Both lasers were operated at 10 Hz. The photolysis and probe lasers were directed into the vacuum chamber and focused onto the molecular beam with 25 and 7.5 cm focal length plano-convex lenses, respectively.

The imaging technique uses an electrostatic immersion lens which serves to extract the ionized $O(^1D)$ fragments from the interaction region and to focus ions with equal velocity vectors to the same point on the detector.³³ The magnification factor of the lens was measured to be 1.17 ± 0.03 by dissociating O_2 and detecting the $O(^3P_2)$ fragment using 2 + 1 REMPI at 225.65 nm.^{36,37} The ionized fragments were accelerated into a field-free flight tube mounted along the axis of the molecular beam. Ions were imaged when they hit a position-sensitive detector consisting of a chevron double microchannel plate (MCP) assembly coupled to a fast phosphor screen (Galileo, P-47). The image on the phosphor screen was recorded by a 640×480 pixel CCD camera (Xybion Electronics, ISG-250U). Both the MCP and camera were electronically gated to collect only signal corresponding to the mass of the $O(^1D)$ fragment. Signal levels were kept below 300 ions per laser shot to avoid saturation of the MCP. The ion counting method was used to increase the spatial resolution of the images.³² About 100 000 total laser shots were added to generate the final image.

III. ANALYSIS

A. Speed distributions

The imaging technique produces a two-dimensional projection of the 3D fragment ion distribution. If the 3D distribution is cylindrically symmetric about an axis in the plane of the detector, then it is possible to mathematically reconstruct the 3D distribution from the 2D projection using the inverse Abel transform.³⁸⁻⁴⁰ Once the 3D distribution is calculated, the speed distribution can be obtained by integrating over all angles at each speed, and the angular distribution can be obtained by integrating over all speeds at each angle. A simple transformation using conservation of linear momentum links the speed and translational energy distributions,

$$|m_{\text{O}}v_{\text{O}}| = |m_{\text{O}_2}v_{\text{O}_2}|, \quad (5)$$

$$\begin{aligned} \text{KE}_{\text{total}} &= \frac{1}{2}m_{\text{O}}v_{\text{O}}^2 + \frac{1}{2}m_{\text{O}_2}v_{\text{O}_2}^2 \\ &= \frac{1}{2}m_{\text{O}}v_{\text{O}}^2 + \frac{1}{2}(2m_{\text{O}})\left(\frac{m_{\text{O}}v_{\text{O}}}{2m_{\text{O}}}\right)^2 = \frac{3}{4}m_{\text{O}}v_{\text{O}}^2. \end{aligned}$$

The internal energy of the O₂ fragment is found from the total kinetic energy distribution using the energy conservation equation,

$$\begin{aligned} \text{KE}_{\text{total}} &= E_{h\nu} - D_0(\text{O}_2(^1\Delta_g) + O(^1D)) \\ &\quad - T(v)_{\text{O}_2} + \text{ZPE}_{\text{O}_2} - E_v(J)_{\text{O}_2}, \end{aligned} \quad (6)$$

where KE_{total} is the total kinetic energy, E_{hν} is the laser energy, D₀ is the dissociation energy, T(v)_{O₂} is the vibrational energy of the O₂(¹Δ_g) fragment, ZPE_{O₂} is the zero point energy of the O₂(¹Δ_g) fragment, and E_v(J)_{O₂} is the rotational energy of the O₂(¹Δ_g) fragment.

B. Angular distributions

Both the spatial anisotropy parameter and the |m_j| distributions can change for the different vibrational modes of the O₂(¹Δ_g) fragment. To account for this we used a semi-continuous parameter method to find the best fit parameters. This method involved breaking the image up into 10 pixel wide rings concentric about the center of the image, and then fitting each region separately. The value of 10 pixels was chosen to approximately average over the rotational levels within one vibrational band.

Upon examining the data (shown in Fig. 1), it is immediately apparent that the O(¹D) fragment from the photodissociation of ozone does not display a 1 + βP₂(cos θ) angular distribution. The origin of the unusual shape of the images lies in the interaction of the ionization laser with the angular momentum of the oxygen atom. By ionizing with linearly polarized light, it is possible to measure the spatial anisotropy parameter and also the relative populations of each |m_j| = 0, 1, or 2 projection. Two fully quantum mechanical methods of extracting the |m_j| distributions of the atomic fragments are used.

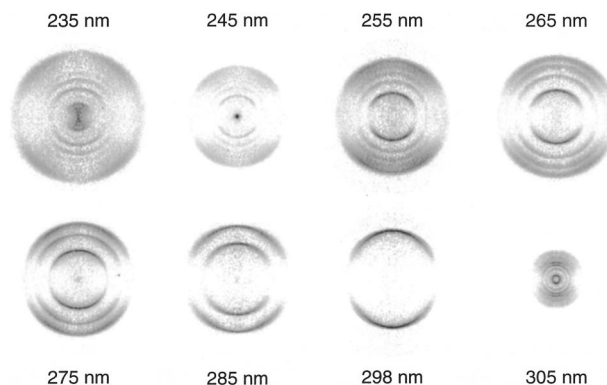


FIG. 1. The inverse Abel transform of the O(¹D₂) photofragment images with both laser polarizations vertical and in the plane of the paper. The dissociation wavelength is shown for each image, but each image is arbitrarily scaled in size. The atoms were ionized via the 205.4 nm 2+1 REMPI process.

1. Diagonal density matrix method

In the first method, we follow Mo and Suzuki's analysis¹⁵ by assuming the ion angular distribution is of the form,

$$I(\theta_d) = I_{\text{dissociation}}(\theta_d) \times I_{\text{detection}}(\theta_d), \quad (7)$$

with

$$I_{\text{dissociation}}(\theta_d) = I(v)[1 + \beta P_2(\cos \theta_d)], \quad (8)$$

while the detection distribution is more complex and depends on the angle between **v** and **J** of the atomic fragment. The angular variable θ_d is used to denote the angle between the velocity of the fragment and the polarization of the dissociation laser. This method assumes that the angular momentum distribution is cylindrically symmetric about the velocity vector of the fragment, and thus it only considers the diagonal elements of the angular momentum density matrix in the molecular frame. Furthermore, the direction of **J** is assumed to be independent of the specific direction **v** in the lab frame. Under these assumptions, the detection probability equations are given as¹⁵

$$I_{\text{detection}}(\theta_d) \propto \sum_K P_K \rho_0^{(K)}(\text{Probe}), \quad (9)$$

$$\begin{aligned} \rho_0^{(K)}(\text{Molecular}) &= \sum_m (-1)^{J-m} \sqrt{2K+1} \\ &\quad \times \begin{pmatrix} J & K & J \\ -m & 0 & m \end{pmatrix} f_m, \end{aligned} \quad (10)$$

where P_K are line strength factors that depend on the specific ionization scheme used, K is the rank of the expansion term, and the f_m are the m_j fractional populations. The ρ₀^(K)(Molecular) are the multipole moments in the molecular frame, and can easily be rotated to the probe frame multipole moments, denoted by ρ₀^K(Probe). Since we are using a linearly polarized, two-photon ionization process, all the odd rank line strength factors are zero in the expansion. While it may not be possible to calculate the line strength factors explicitly, Mo *et al.*²² have shown that the ratio P₀:P₂:P₄ can be

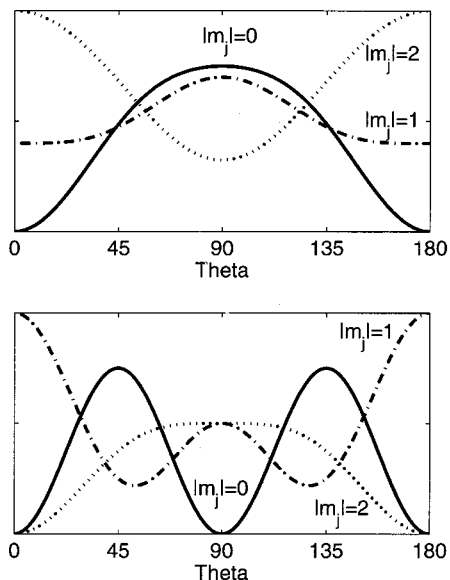


FIG. 2. Ionization probability for the $O(^1F_3) \leftarrow O(^1D_2)$ ionization scheme at 203 nm (top) and the $O(^1P_1) \leftarrow O(^1D_2)$ ionization scheme at 205 nm (bottom).

easily calculated if the initial and final atomic angular momentum states are not equal, i.e., provided $J_i \neq J_f$. When using a two-photon probe, the line strength factors are theoretically nonzero for $K \leq 4$. We calculated the P_K ratios $P_0:P_2:P_4 = 1:0.683:-0.115$ for the 203.7 nm 2+1 REMPI scheme, and $1:-0.598:-1.07$ for the 205.4 nm 2+1 REMPI scheme. These ratios have been reported in other publications as well.^{15,29}

Using the previous equations and the calculated P_K ratios, we can determine the angular shapes of the $I_{\text{detection}}(\theta_d)$ distribution for $|m_j|=0, 1$, or 2. The resulting distributions are shown in Fig. 2. Note that since the ratios of P_K were used, the absolute scale is arbitrary; only the relative shapes and magnitudes are important. We then fit the angular distribution data to a sum of these functions multiplied by the $I_{\text{dissociation}}$ term to obtain the relative $|m_j|$ populations and the β value,

$$I(\theta_d) = P(v)[1 + \beta P_2(\cos \theta_d)] I_{\text{detection}}(\theta_d), \quad (11)$$

with

$$I_{\text{detection}}(\theta_d) = [f_0 F_0(\theta_d) + f_1 F_1(\theta_d) + f_2 F_2(\theta_d)], \quad (12)$$

where f_0, f_1 , and f_2 are the fractional populations of $O(^1D)$ in $|m_j|=0, 1$, and 2, respectively, and $F_0(\theta_d), F_1(\theta_d)$, and $F_2(\theta_d)$ are the corresponding probe frame angular detectivity functions for each magnetic sublevel,

$$\begin{aligned} F_0^{203.7}(\theta_d) &= \frac{3}{4} - \frac{1}{3} \cos^2(\theta_d) - 0.45 \cos^4(\theta_d), \\ F_1^{203.7}(\theta_d) &= \frac{3}{4} - 0.6 \cos^2(\theta_d) - \frac{1}{3} \cos^4(\theta_d), \end{aligned} \quad (13)$$

$$\begin{aligned} F_2^{203.7}(\theta_d) &= \frac{3}{8} + \frac{3}{4} \cos^2(\theta_d) - 0.075 \cos^4(\theta_d); \\ F_0^{205.4}(\theta_d) &= 0 + 3 \cos^2(\theta_d) - 3 \cos^4(\theta_d), \\ F_1^{205.4}(\theta_d) &= \frac{1}{2} - \frac{3}{2} \cos^2(\theta_d) + 2 \cos^4(\theta_d), \\ F_2^{205.4}(\theta_d) &= \frac{1}{2} + 0 \cos^2(\theta_d) - \frac{1}{2} \cos^4(\theta_d). \end{aligned} \quad (14)$$

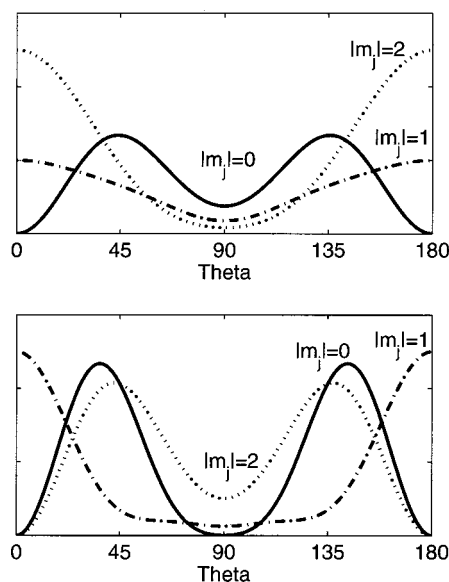


FIG. 3. Ionization probability for the $O(^1F_3) \leftarrow O(^1D_2)$ ionization scheme at 203 nm (top) and the $O(^1P_1) \leftarrow O(^1D_2)$ ionization scheme at 205 nm (bottom), including the $1 + \beta P_2(\cos \theta_d)$ term with $\beta=1.5$.

These detectivity functions were derived for each magnetic sublevel by setting the population of one sublevel equal to 1 while setting the others to zero in Eq. (10), and then solving for the angular shape $I_{\text{detection}}(\theta_d)$ by transforming the multipoles to the probe frame and summing over K .

Since we use the laser geometry where both lasers are parallel and in the plane of the detector, the resultant 3D distributions are cylindrically symmetric about the laser polarization, and thus the angular distribution can be characterized by the single variable θ_d . When plotting the full angular distribution $I(\theta_d) = P(v)[1 + \beta P_2(\cos \theta_d)] I_{\text{detection}}(\theta_d)$, as seen in Fig. 3, we see that the difference between the shapes of the $|m_j|=0$ and $|m_j|=2$ curves is small for the 205.4 nm REMPI scheme. In order to resolve any possible ambiguity between the shapes of different $|m_j|$ curves, we used two different $O(^1D)$ REMPI schemes: one $\{O(^3F) \leftarrow O(^1D)\}$ at 203.7 and one $\{O(^1P) \leftarrow O(^1D)\}$ at 205.4 nm. The shapes of the 203.7 nm REMPI detectivity curves easily distinguish between the $|m_j|=0$ and $|m_j|=2$ levels. Thus, for each dissociation wavelength, we can take one image using each REMPI scheme, and then fit the spatial anisotropy parameter and the $|m_j|$ populations to the angular distributions of both images. This method is valuable because only one laser polarization geometry (both laser polarizations parallel, and in the plane of the detector) is needed in order to obtain the $|m_j|$ populations, β value, and speed distribution. In addition, fitting 1D angular functions is fast and easily done. We used this method at all wavelengths.

2. Full density matrix method

Following the method pioneered by Bracker *et al.*,^{16-18,23,28,41} we can model the 3D angular momentum polarization functions when using linearly polarized light. This model assumes only that \mathbf{J} is cylindrically symmetric about \mathbf{v} . It does not neglect coherence effects, and thus allows for the determination of the full angular momentum

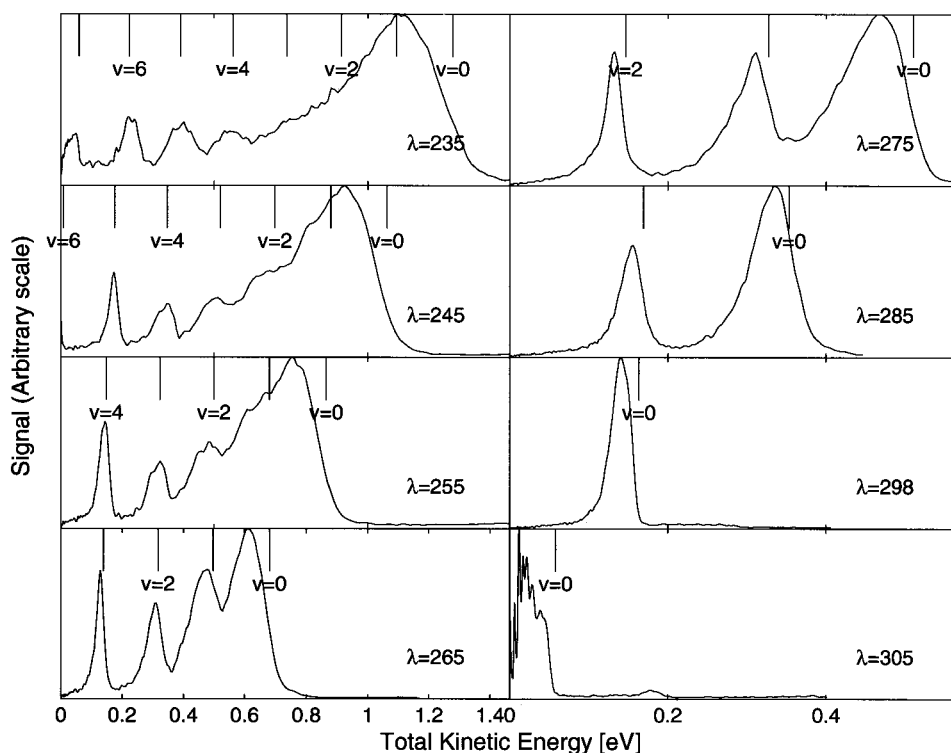


FIG. 4. Total kinetic energy distribution for $O_3 \rightarrow O_2(^1\Delta_g) + O(^1D_2)$. Also shown at each wavelength is a comb corresponding to each vibrational level with no rotational excitation. The peaks observed in the 305 nm image are due to rotational structure. The small peak at ~ 0.19 eV in the 305 nm image is due to an ozone “hot band.”

density matrix as a function of the angle between the photolysis laser polarization and \mathbf{v} . While much of the following analysis has been described elsewhere, is important to outline the basic ideas behind the analysis in order to explain our implementation of the technique. A more detailed explanation is provided in the Appendix.

We again assume that the measured signal has a general form,

$$I = I(v_i) I_{\text{scat}} I_{\text{det}}, \quad (15)$$

with

$$I_{\text{scat}} = [1 + \beta P_2(\cos \theta_d)]. \quad (16)$$

Here, $I(v_i)$ is the speed distribution for each v -level, and $1 + \beta P_2(\cos \theta_d)$ is the standard spatial anisotropy from the dissociation. I_{det} (described more fully in the Appendix) is the detectivity function,

$$I_{\text{det}}(a_q^{(2)}(p), \beta, s_2, \theta_d, \Theta, \Phi), \quad (17)$$

where the $a_q^{(k)}(p)$ are the alignment parameters, with p denoting either a parallel or perpendicular transition. S_2 is the line strength factor,⁴² and the additional angles are defined in Eq. (A9).

The rank 2 parameters $a_q^{(k)}(p)$ are found by fitting the data images I_{iso} and I_{aniso} to basis functions $B_{x,y,z}^F[\beta, a_q^{(k)}(p)]$ using the fit parameters c_i and $a_q^{(k)}(p)$ in the following equations:¹⁸

$$I_{\text{iso}}^F = \sum_i c_i^F B_{\text{iso}}^F(v_i) I_{\text{aniso}}^F, \quad (18)$$

$$I_{\text{aniso}}^F = s_2 \sum_{i,q,p} c_i^F b_q^{(2)}(p) B_{\text{aniso}}^F[b_q^{(k)}(p); v_i],$$

for each dissociation laser polarization direction F (along \mathbf{x} , \mathbf{y} or \mathbf{z}). Here, the data images I_{iso} and I_{aniso} are defined as

$$I_{\text{iso}}^F = \langle N_x^F \rangle + \langle N_y^F \rangle + \langle N_z^F \rangle, \quad (19)$$

$$I_{\text{aniso}}^F = N_z^F - N_y^F, \quad (20)$$

where x , y , and z refer to the ionization laser polarization direction, and N_z^F are the normalized data images, as described in the Appendix. The brackets $\langle \rangle$ indicate a sum over the intensities of all pixels in the image. The basis functions are defined as

$$B_{\text{iso}}^F = 3I(v_i)[1 + \beta P_2(\cos \theta_d)], \quad (21)$$

$$B_{\text{aniso}}^F[\beta, a_q^{(k)}(p)] = B_z^F[\beta, a_q^{(k)}(p)] - B_y^F[\beta, a_q^{(k)}(p)], \quad (22)$$

with the expression for $B_{x,y,z}^F[\beta, a_q^{(k)}(p)]$ given in Eq. (A17). Once the rank 2 parameters are found, we fit to β in the following expression:

$$N_{y,z}^F = \sum_i c_{y,z}^F(i) \left\{ I(v_i) + I(v_i) \beta_i P_2^F(\cos \theta) + s_2 \left[\sum_{q,p} a_q^{(2)}(p) \mathbf{B}_{y,z}^F[a_q^{(2)}(p); v_i] \right] \right\}, \quad (23)$$

where the $a_q^{(2)}(p)$ are fixed from the previous fit, and the $c_{y,z}^F(i)$ are theoretically the same as the c_i^F , but are now allowed to vary because of the addition of the rank zero $1 + \beta P_2(\cos \theta_d)$ term.

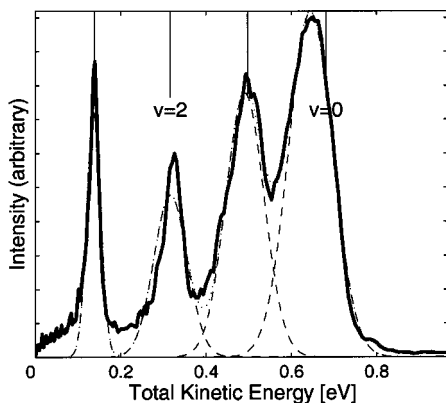


FIG. 5. Photofragment energy distribution from the dissociation process at 265 nm using the 203 nm ionization scheme. Gaussian fits to the vibrational peaks are shown as dotted lines.

IV. RESULTS

Inverse Abel transformed images are shown in Fig. 1 for various dissociation wavelengths using the 205.4 nm REMPI scheme. The images that used the 203.7 nm probe had similar radial distributions but slightly different angular distributions from the ones shown. It is important to note that the true nascent angular distribution of the $O(^1D_2)$ fragments has a shape characterized by $1 + \beta P_2(\cos \theta_d)$. Any deviation from that shape is due to the variation in ionization probability caused by the atomic alignment. Although it is possible for the atomic alignment and thus the integrated ionization probability to change with radius, we assumed that the overall effect of any changes in alignment on the vibrational populations was small. This assumption is justified by the small change in atomic alignment as a function of speed in our measurements. In principle, the full density matrix method allows one to adjust the vibrational populations to produce a better fit of vibrational populations, but due to the already large parameter set of the data at 255 nm, we did not explore that possibility. The corresponding energy distribution for each wavelength is shown in Fig. 4. Structure

in the 305 nm dissociation result is due to individual rotational levels within the $v=0$ level of the $O_2(^1\Delta_g)$ molecule.

In order to obtain the vibrational populations, Gaussians were fit to each vibrational peak and then integrated to determine the relative population of that peak relative to the whole curve. An example of this process is shown in Fig. 5 for the 265 nm dissociation. We recognize that the Gaussians sometimes do not accurately represent the vibrational populations due to the tail on the high energy side of the vibrational peak that sometimes extends beyond the $j=0$ energy. Some signal may extend to higher energies than the theoretical limit due to our finite experimental resolution and/or space charge effects, etc. For most peaks, the fit is sufficient. The vibrational populations are shown in Table I along with the populations reported by other research groups. Vibrational populations for $v=0$ and 1 at 235 and 245 nm are only estimates due to our inability to properly separate the two vibrational modes.

Angular distributions and fits at 265 nm are shown in Fig. 6 for the 203 and 205 nm schemes. The curves shown represent the angular distribution obtained at the maximum of the $v=0$ and $v=3$ peaks; the angular distributions at other energies have a similar signal to noise ratio, but different shapes. Since regions with low ion counts between the vibrational peaks contribute less to the total image signal and also contain more noise due to counting statistics, the best angular fit parameters for each vibrational level were determined at the peak of the fit for each vibrational level. Best angular fit parameters are shown in Table II. Also shown in Table II are results using the full density matrix method and any other published results. Anisotropy parameter errors are assumed to be $\pm 10\%$.

$O(^1D_2)$ alignment results using the “diagonal matrix method” are shown in Table III. The numbers reported as “average” were determined by calculating one speed-averaged angular distribution, and then finding the best fit to that data. Since the probe used a linearly polarized 2 + 1 REMPI technique, the experiment does not measure the

TABLE I. Vibrational populations of $C_2(^1\Delta_g)$ from the photodissociation of ozone with light of wavelength λ .

λ (nm)	$v=0$	$v=1$	$v=2$	$v=3$	$v=4$	$v=5$	$v=6$	$v=7$	Source
235	30%	24%	15%	7%	7%	7%	5%	6%	This work
240	64%	15%	8%	4%	5%	4%	2%		Reference 6
245	34%	23%	20%	8%	8%	4%	0%		This work
248	49%	15%	15%	8%	8%	5%			Reference 5
248	65%	18%	8%	5%	3%	4%			Reference 6
255	39%	30%	14%	10%	8%				This work
265	44%	32%	14%	10%					This work
266	52%	27%	14%	7%					This work ^a
266	57%	24%	12%	7%					Reference 2
266	59%	22%	12%	7%					Reference 6
275	59%	26%	15%						This work
275	61%	27%	12%						Reference 5
280	70%	30%							Reference 5
280	70%	22%	8%						Reference 6
285	71%	29%							This work
285	76%	24%							Reference 5
293	76%	24%							Reference 6

^aOnly one image was taken at this wavelength using the 205 nm ionization scheme.

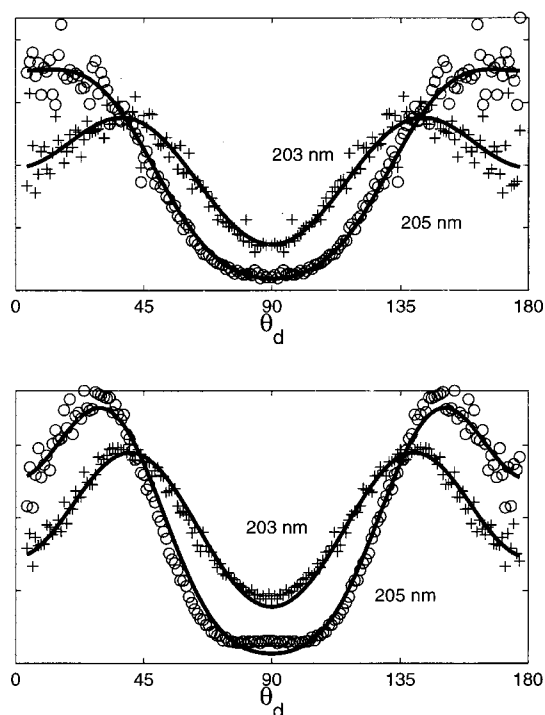


FIG. 6. Angular distribution and fits for the $v=0$ (top) and $v=3$ (bottom) peak in the 265 nm energy distribution. The two curves in each figure represent angular distributions from different $O(^1D_2)$ ionization schemes.

sign of $|m_j|$. Orientation (+ versus $-m_j$) measurements would require a circularly polarized beam.

A. Results at 305.7456 nm

The rotational structure observed within the $v=0$ band requires a more detailed analysis. In a previous study of the ozone dissociation energy,⁴³ the 305.7456 nm image and energy distribution were presented in Figs. 1 and 4 of that reference, respectively. This previous publication also describes the details of assigning the rotational lines. Here, we

concentrate on the spatial anisotropy parameter and alignment as a function of the $O_2(^1\Delta_g)$ rotational level.

Due to the complexity of the energy distribution, no population fits were performed. In order to understand the interesting structure that seems to be dependent on the angular momentum of the $O_2(^1\Delta_g)$ fragment, we used the rotational assignments to extract the angular distribution for each peak. Each of these angular distributions was then analyzed using the diagonal density matrix method in the same fashion as the vibrational levels in the previous section. The results are tabulated along with the corresponding spatial anisotropy parameters in Table IV. The results for the rotational states $j=0$ through $j=6$ are averaged because of our inability to resolve peaks in this region.

B. Full density matrix results

Data were acquired at 255 and 298 nm in order to determine the full density matrix. The wavelength of 298 nm was chosen because it contained only one well-defined vibrational level, making the analysis “easy.” Figure 7 shows the four images acquired at the 255 nm dissociation wavelength. Note the strong change in the shape of the images as the ionization laser changes. If there were no rank 2 vector correlations, the images would not depend on the ionization laser polarization. Images for the 298 nm dissociation are similar, and will be described later (Fig. 9).

The rank 2 alignment parameters are found by fitting the subtraction images $I_{\text{aniso}}^F = N_z^F - N_y^F$ to the $a_q^{(k)}(p)$ dependent basis functions. The best fit results are shown in Fig. 8 for 298 nm. The 255 nm results are similar, but have a smaller residual (Data-Fit). The numerical results from the rank 2 alignment parameter fits are presented in Tables V and VI. Both the $b_q^{(k)}(p)$ and the $a_q^{(k)}(p)$ parameters are shown here because the basis functions are linear in $b_q^{(k)}(p)$, making it easier to understand the true weighting of the basis functions in the fit. The $a_q^{(k)}(p)$ are shown in order to compare with other results.

TABLE II. Anisotropy parameter β results and comparison with results from other research groups.

λ (nm)	Beta								Avg.	Source	Comments
	$v=0$	$v=1$	$v=2$	$v=3$	$v=4$	$v=5$	$v=6$	$v=7$			
230									1.12	4	
235	1.1	1.19	1.21	1.15	1.00	0.84	0.57	0.71	0.80		
245	1.3	1.28	1.23	1.15	1.08	1.03			1.16		
248	1.25	1.25	1.25	1.25	1.25	1.6				5	
248									1.2	8	Qualitative
255	1.2	1.33	1.28	1.35	1.32				1.03		
	1.2 ^a	1.4 ^a	1.4 ^a	1.2 ^a	1.1 ^a						
265	1.5	1.46	1.27	1.37					1.39		
266									1.11	4	
275	1.6	1.5	1.5						1.49		
270–300									1.6 \pm 0.2	5	
274–300									1.2 \pm 0.2	1	Effusive beam
285	1.8	1.6							1.46		
294.5									1.45		
298									1.71		
									1.7 ^a		

^aFull density matrix method.

TABLE III. $O(^1D_2)|m_j\rangle$ populations using the diagonal matrix method corresponding to different vibrational states of $O_2(^1\Delta_g)$. The populations were found at the peak of the Gaussian fit for each vibrational level. The average $|m_j\rangle$ populations for the whole image are shown in the right column.

λ (nm)	Populations									
	$v=0$	$v=1$	$v=2$	$v=3$	$v=4$	$v=5$	$v=6$	$v=7$	Avg.	
235	$ m_i =0$	71%	74%	74%	68%	56%	44%	31%	29%	57%
	$ m_i =1$	20%	18%	19%	24%	32%	45%	43%	42%	30%
	$ m_i =2$	9%	8%	7%	8%	12%	12%	26%	28%	14%
245	$ m_i =0$	65%	69%	63%	56%	48%	50%			60%
	$ m_i =1$	29%	27%	33%	41%	47%	39%			34%
	$ m_i =2$	6%	5%	4%	4%	5%	11%			6%
255	$ m_i =0$	59%	65%	60%	51%	57%	57%			76%
	$ m_i =1$	39%	34%	40%	43%	40%	20%			23%
	$ m_i =2$	1%	1%	0%	6%	2%	2%			0%
265	$ m_i =0$	62%	65%	62%	52%					60%
	$ m_i =1$	34%	32%	31%	44%					35%
	$ m_i =2$	4%	3%	8%	5%					5%
275	$ m_i =0$	67%	70%	52%						63%
	$ m_i =1$	32%	29%	47%						35%
	$ m_i =2$	1%	1%	1%						1%
285	$ m_i =0$	74%	79%							77%
	$ m_i =1$	26%	21%							23%
	$ m_i =2$	0%	0%							0%
294.5	$ m_i =0$	52%	24%							42%
	$ m_i =1$	47%	45%							46%
	$ m_i =2$	1%	31%							12%
298	$ m_i =0$	48%								45%
	$ m_i =1$	49%								50%
	$ m_i =2$	3%								6%
305	$ m_i =0$									28%
	$ m_i =1$									49%
	$ m_i =2$									24%

It is also possible to calculate the full density matrices from the measured rank 2 alignment parameters at 255 and 298 nm. We found, however, that the best fit results at 255 nm overemphasized the $a_0^{(2)}(\parallel)$ term, yielding negative elements in the density matrix. This is likely due to the neglect of the rank 4 terms in our model. Thus, the rank 2 results should be considered qualitative in nature. With this caveat, the full density matrices for the 298 nm data are reported here for different lab angles (0° , 45° , and 90°) between the dissociation laser polarization and the velocity of the $O(^1D)$ fragment,

$$\rho_{m'm}^{0^\circ} = \begin{pmatrix} 0.06 & 0 & 0 & 0 & 0 \\ 0 & 0.27 & 0 & 0 & 0 \\ 0 & 0 & 0.37 & 0 & 0 \\ 0 & 0 & 0 & 0.27 & 0 \\ 0 & 0 & 0 & 0 & 0.06 \end{pmatrix} \quad (24a)$$

(i.e., \mathbf{v} parallel to the dissociation laser polarization)

TABLE IV. Anisotropy and β results for 305.7456 nm.

	$J=16$	15	14	13	12	11	10	9	8	7	Avg. (6-0)	Avg.
β	0.13	0.57	0.75	1.1	1.5	1.5	1.6	1.6	1.7	1.7	1.29	1.13
$ m_j =0$	0.11	0.17	0.27	0.25	0.11	0.50	0.44	0.24	0.22	0.39	0.29	0.28
$ m_j =1$	0.47	0.43	0.45	0.49	0.63	0.33	0.46	0.59	0.53	0.50	0.53	0.48
$ m_j =2$	0.42	0.39	0.28	0.25	0.26	0.16	0.10	0.16	0.24	0.11	0.18	0.23

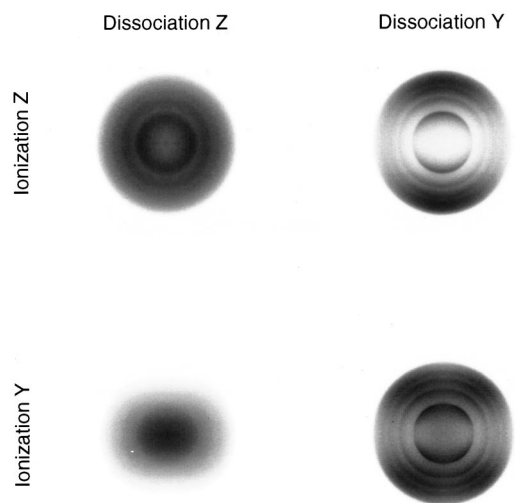


FIG. 7. Raw images from the 255 nm dissociation of ozone using the 203 nm ionization scheme for different dissociation and ionization laser polarizations.

$$\rho_{m'm}^{45^\circ} = \begin{pmatrix} 0.06 & 0.11 & 0.01 & 0 & 0 \\ 0.11 & 0.27 & 0.04 & 0.01 & 0 \\ 0.01 & 0.04 & 0.34 & -0.04 & 0.01 \\ 0 & 0.01 & -0.04 & 0.27 & -0.11 \\ 0 & 0 & 0.01 & -0.11 & 0.06 \end{pmatrix} \quad (24b)$$

$$\rho_{m'm}^{90^\circ} = \begin{pmatrix} 0.10 & 0 & 0.14 & 0 & 0 \\ 0 & 0.25 & 0 & 0.17 & 0 \\ 0.14 & 0 & 0.30 & 0 & 0.14 \\ 0 & 0.17 & 0 & 0.25 & 0 \\ 0 & 0 & 0.14 & 0 & 0.10 \end{pmatrix} \quad (24c)$$

(i.e., \mathbf{v} perpendicular to the dissociation laser polarization).

The full density matrices for other wavelengths or angles can be calculated using Eq. (A21). The calculated $|m_j|$ popu-

TABLE V. $b_q^{(k)}(p)$ results from fitting the second-rank alignment parameters.

λ (nm)	$b_0^{(2)}(\parallel)$	$b_0^{(2)}(\perp)$	$b_1^{(2)}(\parallel, \perp)$	$b_2^{(2)}(\perp)$	Beta
255 $v=0$	-1.7	-0.17	0.52	-0.08	1.22
$v=1$	-2.1	-0.01	-0.05	-0.02	1.37
$v=2$	-2.1	-0.15	-0.23	0.02	1.42
$v=3$	-1.8	-0.22	-0.05	0.14	1.21
$v=4$	-1.6	-0.22	-0.01	-0.02	1.05
298 $v=0$	-1.3	-0.05	0.87	0.07	1.70

lations are shown in Table VII for $\theta_d=0^\circ$. Once the rank 2 parameters are known, it is possible to fit the spatial anisotropy parameter β . The quantitative results from these fits are shown in Table II. The image fit results are shown in Fig. 9 for the 298 nm dissociation.

V. DISCUSSION

A. Introduction and vibrational populations

In spite of the many studies of the photodissociation of ozone in the Hartley band, we still lack a complete understanding of the dissociation dynamics. Researchers have struggled to explain the structure on top of the Hartley band,^{10,44,45} and the complexity of the ozone molecule has provided interesting experimental results. For example, reaction (2) is known to form highly excited $O_2(^3\Sigma_g^-)$ molecules,⁴⁶ and Thelen *et al.* recently demonstrated a large fluctuation in $O_2(^1\Delta_g)$ vibrational populations from reaction (1) between 272.8 and 285.6 nm.⁵ Measurements done by Thelen *et al.* at 275 and 285 nm agree nicely with ours. While the results from Valentini *et al.* are in agreement that

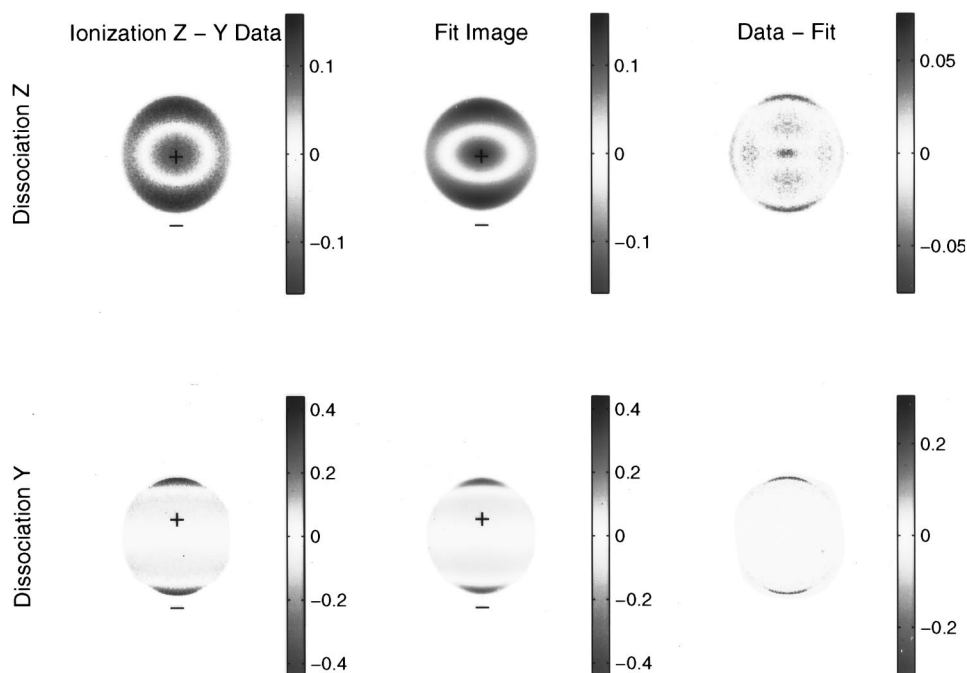


FIG. 8. Rank 2 fits for 298 nm photodissociation of ozone. Column 1 shows the subtraction image data, and the fit and residual are shown in columns 2 and 3, respectively.

TABLE VI. $a_q^{(k)}(p)$ results from fitting the second-rank alignment parameters.

λ (nm)	$a_0^{(2)}(\parallel)$	$a_0^{(2)}(\perp)$	$a_1^{(2)}(\parallel, \perp)$	$a_2^{(2)}(\perp)$	Beta
255 $v=0$	-0.77	-0.43	0.52	-0.20	1.22
$v=1$	-0.91	-0.04	-0.05	-0.08	1.37
$v=2$	-0.88	-0.53	-0.23	0.07	1.42
$v=3$	-0.81	-0.56	0.05	0.35	1.21
$v=4$	-0.77	-0.46	-0.01	-0.03	1.05
298 $v=0$	-0.49	-0.34	0.87	0.50	1.70

most population is in the lowest vibrational levels, they indicate consistently more population in $v=0$ than either our results or those of Thelen *et al.* Theoretical predictions by Leforestier *et al.*¹⁰ agree that most population is in the lowest vibrational levels.

B. Anisotropy parameter

Our measurements of the anisotropy parameter show an increase with respect to wavelength, whereas other data summarized in Table II do not, at first, appear to show this trend. It is important, however, to recognize that the measurements of Fairchild *et al.* were performed using an effusive source, so that the ozone molecules were not rotationally cold. High rotational temperatures can significantly decrease the spatial anisotropy parameter β .²⁴ The results from Takahashi *et al.* were performed in a reaction cell, and thus the initial ozone molecules were also not rotationally cold. These researchers accounted for the high rotational temperature, but it is possible that the correction added additional error to the final value. Most promising are the recent supersonic expansion results from Thelen *et al.*, which agree well with ours.

The spatial anisotropy parameter is directly related to the bond angle at the time of dissociation. If the excited state of ozone were to dissociate from the same bond angle as the ground state, 116.8°, the β value would be 1.18. This value compares favorably with our shorter wavelength results. However, at longer wavelengths, there is a trend toward much higher β values, approaching the parallel limit of 2 near 305 nm. This implies a large change in the bond angle during the dissociation at longer wavelengths. For comparison, $\beta=1.9$ corresponds to a bond angle of 159° at the time of dissociation. This large geometry change may not be too surprising since wavepacket calculations on ozone photodissociation^{10,47} show that there is significant activity in the bending and stretching modes during the photodissociation process. Although the trajectory plots in Fig. 11 of Ref. 10 do not extend far enough in time to determine the final

TABLE VII. $O(^1D)|m_j|$ populations at 298 and 255 nm for $\theta_d=0^\circ$.

	$m_j=0$	$m_j=1$	$m_j=2$
298 nm	34%	54%	12%
255 nm $v=0$	42%	62%	-4%
255 nm $v=1$	46%	66%	-12%
255 nm $v=2$	45%	65%	-10%
255 nm $v=3$	43%	63%	-6%
255 nm $v=4$	42%	62%	-5%

bond angle, those in Fig. 14 of Ref. 47 show that the hyperspherical coordinates θ and φ approach $\pi/2$ and 0, respectively, corresponding to an opening of the O–O–O bond angle toward 180°. This agrees qualitatively with our observations.

C. Dependence of β on $O_2(^1\Delta_g)$ vibration and rotation

We also considered the change in β with vibrational level for dissociation at a given wavelength. In general, there is not a clear change in β with vibration level of the $O_2(^1\Delta_g)$ fragment, at least not one that is consistent at all wavelengths. Within the rotational structure of the 305.7456 nm image, the spatial anisotropy parameter clearly rises from near 0 at the lowest translational energies to near 1.8 at the highest ones. Other groups have measured rotationally dependent anisotropy parameters as a function of rotation of the counterfragment from the photodissociation of OCS (Refs. 30, 48, 49) and N_2O .²⁶ Kim *et al.* previously analyzed the spatial anisotropy parameter β of $S(^1D)$ from the photodissociation of OCS and attributed the change in β to a mixed transition for the higher speed fragments, and a pure parallel transition for the slower fragments. These results were justified by also measuring the coherence term $\text{Im}[a_1^{(1)}(\parallel, \perp)]$, which showed an increase at higher speeds, indicative of competition between different states. Neyer *et al.* studied the $O(^1D_2)$ fragment from the photodissociation of N_2O , also finding a change in β with respect to the photofragment speed. The different speeds of the $O(^1D_2)$ fragment corresponded to different rotational states of the N_2 fragment, with $\beta \approx 0.2$ for the slowest ($J=80$) fragments, and $\beta \approx 2$ for the fastest ($J=50$) fragments. This change was explained in terms of the branching between the $2^1A'$ and $1^1A''$ electronic states during dissociation. It is possible, however, that our observed changes in β may be explained more simply. Fragments that dissociate very near threshold take longer to break apart, allowing the parent molecule to rotate during the dissociation. Using the axial recoil velocities as a guide, a calculation shows that for slow fragments photodissociated at 305 nm, the ozone molecule rotates significantly during the dissociation process. Perhaps more importantly, the axial recoil approximation, an assumption implicit in all of the analysis, breaks down for very slow fragments.

D. M_j populations (diagonal method)

The rank 2 alignment results show a consistent preference for low $|m_j|$ states, with little or no population in the $|m_j|=2$ states. In general, the diagonal density matrix method finds most population in the $|m_j|=0$ states, some in the $|m_j|=1$, and almost none in the $|m_j|=2$ states. It seems that there is a slight trend toward more $|m_j|=0$ population for faster (lower vibration) fragments, but this trend is not strong. At 305.7456 nm, we see a trend toward more $|m_j|=0$ at higher kinetic energies (lower J). This feature is similar to the results reported by Neyer *et al.* for the alignment of $O(^1D_2)$ from N_2O .²⁶

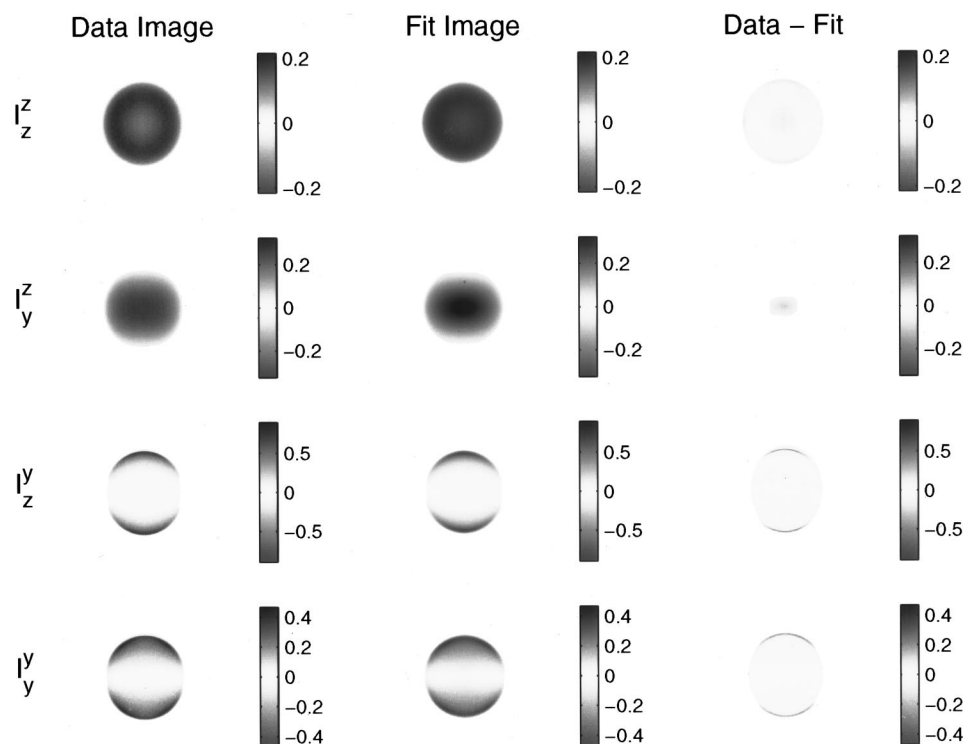


FIG. 9. Spatial anisotropy parameter β fit results for 298 nm photodissociation of ozone.

It is very difficult to predict the $|m_j|$ population for the dissociation of ozone. Many states of the atom+diatom in C_s symmetry lie at lower energies than the energy of the ozone D state in C_{2v} geometry, and there is no obvious choice as to which should correlate with the excited state. Perhaps the simplest explanation for the observed result is one of conservation of symmetry. The ozone transition starts (in C_s symmetry) from an A' state, and the high measured values of β show that it must also reach an A' state. If the atomic product maintains this A' symmetry with respect to the plane containing the oxygen molecule and the recoil velocity, then we would expect the m_j distribution to favor A' symmetry. The orbital symmetry for $m_j=0$ has A' symmetry, while those for $|m_j|=1$ and $|m_j|=2$ have one component each of A' and A'' symmetry. Thus, it is not surprising that the overall $|m_j|$ distribution should favor $|m_j|=0$.

E. Full density matrix results

Results from the full density matrix method show a clear preference for a parallel, incoherent dissociation mechanism with little perpendicular character and differing levels of coherent character. The large number of fit parameters in the 255 nm data led to a best fit which resulted in $b_q^{(k)}(p)$ that were too large $\{\text{abs}(b_0^{(2)}(\parallel)) > 1.7\}$, making the $|m_j|=2$ portion of the density matrix negative. We believe that the lack of rank 4 terms in the analysis led to this result. While the rank 4 line strength factor is small, it is essential to include those terms in the diagonal density matrix method. Without the rank 4 terms in the full density matrix method, "extra" rank 2 signal is needed in the fit to compensate. For this reason, we believe the full density matrix results to be qualitative in nature, but they nonetheless suggest a strong preference at both 255 and 298 nm for angular momentum align-

ment arising from a parallel, incoherent photodissociation. The $|m_j|$ distributions (diagonal part of the density matrix) from this method are thus not emphasized, but are shown for the 298 nm photodissociation where the best fit results yielded real values for the density matrix. The full density matrices for other wavelengths or angles can be calculated using Eq. (A21). When looking at the diagonal elements of the density matrices from the 298 nm photodissociation process, it is noticeable that they do not show a large change as a function of angle between the photolysis laser polarization and the velocity of the $O(^1D_2)$ fragment. This validates the assumption in the diagonal matrix method that the angular momentum distribution is independent of angle.

Even though the rank 2 alignment parameter results may be qualitative, the spatial anisotropy parameter fit is a valid result. The β parameter can only be inaccurately measured if the residual from the higher-order fit is large. This is due to the rank 2 alignment parameters' dependence only on signal that is independent of the rank 0 part of the data. These ideas are confirmed by the excellent agreement of the spatial anisotropy parameter β in the two different methods.

F. The dissociation mechanism

The data presented here on the $O_2(^1\Delta_g) + O(^1D_2)$ dissociation channel are consistent with a mechanism in which excitation takes place to a state of A' symmetry that then dissociates on a time scale rapid compared to rotation. This view is supported by the large values found for β , consistent with a parallel transition from the A' ground state, and by the alignment of the $O(^1D_2)$, where the propensity for the A' $m_j=0$ state would be the result of conservation of symmetry. The large values of β also indicate that substantial bending

of ozone occurs prior to dissociation, in agreement with recent theoretical predictions.^{10,47} The increase of the anisotropy parameter with wavelength indicates that higher wavelengths result in more significant bending toward the linear configuration than do shorter wavelengths. The dominance of $v=0$ population at all wavelengths is consistent with the previously proposed model of a rotationally impulsive but vibrationally adiabatic dissociation mechanism.⁶ Finally, the full density matrix results show that the dissociation has a clear preference for a parallel, incoherent dissociation mechanism expected for excitation to a single dissociative state of A' symmetry.

VI. CONCLUSION

We have measured several aspects of the photodissociation of ozone in the wavelength range 235–305 nm yielding $O(^1D_2) + O_2(^1\Delta_g)$. The vibrational populations of $O_2(^1\Delta_g)$ are peaked at $v=0$ for all wavelengths, and all vibrationally-accessible states are at least partially filled. A diagonal density matrix method was used to study the alignment and spatial anisotropy of the $O(^1D_2)$ fragment. The value of β varied from about 1.2 at 235 nm to 1.7 at 298 nm. The $|m_j|$ populations were peaked at $|m_j|=0$, with some population in $|m_j|=1$, and very little in $|m_j|=2$. These results were generally confirmed by the larger data sets taken at 255 nm and 298 nm, where four different laser polarization combinations were used in order to determine the full density matrix, albeit with only rank 0 and 2 terms. The $|m_j|$ distributions using this method were more peaked at $|m_j|=1$, yet still maintained the lack of population in $|m_j|=2$. The results also illustrated a clear preference for incoherent, parallel excitation. Dissociation of ozone to $O(^1D_2) + O_2(^1\Delta_g)$ takes place after excitation to a state of A' symmetry and after substantial bending of the parent molecule.

ACKNOWLEDGMENTS

The authors thank Dr. Julie Mueller for her help setting up this experiment, and Dr. Eloy Wouters, Professor Greg Hall, Professor Oleg S. Vasyutinskii, and Professor Barry Carpenter for their useful insight and discussions. This work was supported by the National Science Foundation under Grant No. CHE-9901065.

APPENDIX

1. Fitting process overview

The general fitting process is as follows: First, isolate the rank 2 part of the images by subtracting two images with different ionization laser polarizations and the same dissociation laser polarization. This results in an image that does not contain the rank zero $[1 + \beta P_2(\cos \theta_d)]$ term. Then, fit this “subtraction” image to a sum of basis functions that each depend linearly on one of the rank 2 angular momentum functions. The rank 2 alignment parameters are the results of this fit. Once the rank 2 alignment parameters are determined, this effectively provides ionization probability or modulation of the original $[1 + \beta P_2(\cos \theta_d)]$ photofragment

distribution. Using this information, one can then fit for β in a more general expression that includes the rank zero and higher order terms.

2. Notation

Images $I_{x,y,z}^F$ will be labeled with a superscript F denoting the polarization direction of the dissociation laser, and a subscript denoting the polarization direction of the ionization laser. In our apparatus, the z -axis is perpendicular to the MCP detector face, and the y -axis is in the plane of the detector and perpendicular to the plane defined by the propagation directions of the laser and molecular beams.

3. Normalization

When analyzing several images at once, it is important that all the data images are taken under identical conditions except for the laser polarization. In practice, fluctuations in the laser power and the overlap between the two laser beams influences the total signal detected. A given data image $I_{x,y,z}^F$ therefore must be normalized appropriately when comparing it with others.¹⁷ For example, if we define

$$M_{x,y,z}^F \equiv \frac{I_{x,y,z}^F}{\langle I_{x,y,z}^F \rangle}, \quad (A1)$$

where the brackets $\langle \rangle$ indicate a sum over the intensities of all pixels in the image, and then define

$$\left(\frac{I_{\parallel}}{I_{\perp}} \right)^{(z)} \equiv \frac{\langle I_z^z \rangle}{\langle I_y^z \rangle}, \quad (A2)$$

and

$$\left(\frac{I_{\parallel}}{I_{\perp}} \right)^{(y)} \equiv \frac{\langle I_y^y \rangle}{\langle I_z^y \rangle}, \quad (A3)$$

then the following images are properly normalized:

$$N_y^z = M_y^z = \frac{I_y^z}{\langle I_y^z \rangle} \quad \text{and} \quad N_z^z = \left(\frac{I_{\parallel}}{I_{\perp}} \right)^z M_z^z = \frac{\langle I_z^z \rangle}{\langle I_y^z \rangle} \frac{I_z^z}{\langle I_z^z \rangle} \quad (A4)$$

for the dissociation laser polarization along z , and

$$N_y^y = \left(\frac{I_{\parallel}}{I_{\perp}} \right)^y M_y^y = \frac{\langle I_y^y \rangle}{\langle I_z^y \rangle} \frac{I_y^y}{\langle I_y^y \rangle} \quad \text{and} \quad N_z^y = M_z^y = \frac{I_z^y}{\langle I_z^y \rangle} \quad (A5)$$

for the dissociation laser polarization along y . The constant I_{\parallel}/I_{\perp} (usually close to 1) can either be measured directly or determined in the fitting procedure. These normalized versions of the data images $N_{y,z}^F$ are used throughout the analysis.

4. Analysis

To model the intensity distribution, we again assume that the measured signal has a general form,

$$I = I(v_i) I_{\text{scat}} I_{\text{det}}, \quad (A6)$$

with

$$I_{\text{scat}} = [1 + \beta P_2(\cos \theta_d)] \quad (A7)$$

and

$$I_{\text{det}} = 1 + s_2 \{ (1 + \beta) a_0^{(2)}(\parallel) \cos^2 \theta_d P_2(\cos \theta_d) + (1 - \beta/2) a_0^{(2)}(\perp) \sin^2 \theta_d P_2(\cos \theta_d) \\ + \text{Re}[a_1^{(2)}(\parallel, \perp)] \sqrt{3/2} \sin \theta_d \cos \theta_d \sin 2\Theta \cos \Phi + (1 - \beta/2) a_2^{(2)}(\perp) \sqrt{3/2} \sin^2 \theta_d \sin^2 \Theta \cos 2\Phi \} / [1 + \beta P_2(\cos \theta_d)]. \quad (\text{A8})$$

Here $I(v_i)$ is the speed distribution for each v -level, and $1 + \beta P_2(\cos \theta_d)$ is the standard spatial anisotropy from the dissociation. The $a_q^{(k)}(p)$ are the alignment parameters, with p denoting either a parallel or perpendicular transition. S_2 is the line strength factor.⁴² The angles are defined as

$$\begin{aligned} \cos \theta_d &= \hat{\epsilon}_{\text{phot}} \cdot \hat{v}, \\ \cos \Theta &= \hat{\epsilon}_{\text{probe}} \cdot \hat{v}, \\ \cos \Phi &= \frac{P_{\text{phot}} \cdot P_{\text{probe}}}{|P_{\text{phot}}| |P_{\text{probe}}|} = \frac{(\hat{\epsilon}_{\text{phot}} - \cos \theta_d \hat{v}) \cdot (\hat{\epsilon}_{\text{probe}} - \cos \Theta \hat{v})}{|\hat{\epsilon}_{\text{phot}} - \cos \theta_d \hat{v}| |\hat{\epsilon}_{\text{probe}} - \cos \Theta \hat{v}|}. \end{aligned} \quad (\text{A9})$$

Note that the quantity $I_{\text{iso}} = \langle N_x \rangle + \langle N_y \rangle + \langle N_z \rangle$ is proportional to $1 + \beta P_2(\cos \theta_d)$, and the quantity $I_{\text{aniso}}^F = N_z^F - N_x^F$ is independent of the $1 + \beta P_2(\cos \theta_d)$ term, depending only on the second-rank terms (fourth-rank terms are neglected). By comparing I_{aniso}^F with the appropriate basis functions, we are able to determine the rank two alignment parameters. The basis functions are defined as

$$B_{x,y,z}^F[\beta, a_q^{(k)}(p)] = I(v) s_2 \{ (1 + \beta) a_0^{(2)}(\parallel) \cos^2 \theta_\epsilon P_2(\cos \theta_\epsilon) + (1 - \beta/2) a_0^{(2)}(\perp) \sin^2 \theta_\epsilon P_2(\cos \theta_\epsilon) \\ + \text{Re}[a_1^{(2)}(\parallel, \perp)] \sqrt{3/2} \sin \theta_\epsilon \cos \theta_\epsilon \sin 2\Theta \cos \Phi + (1 - \beta/2) a_2^{(2)}(\perp) \sqrt{3/2} \sin^2 \theta_\epsilon \sin^2 \Theta \cos 2\Phi \}. \quad (\text{A10})$$

In order to solve for all the unknown parameters, we first construct individual basis functions

$$B_{\text{iso}}^F = 3I(v)[1 + \beta P_2(\cos \theta_d)], \quad (\text{A11})$$

which will be compared with the quantity,

$$I_{\text{iso}}^F = N_x^F + N_y^F + N_z^F, \quad (\text{A12})$$

such that we solve for the constant c_i^F in the following expression:

$$I_{\text{iso}}^F = \sum_i c_i^F B_{\text{iso}}^F(v_i), \quad (\text{A13})$$

where the possible dependence on a given vibrational level v_i has been left in explicitly. This constant c_i^F is just the ratio between the basis functions and the data.

In practice, it not simple to set-up an experiment which can easily change the ionization laser polarization to measure all three (x,y,z) images. In our apparatus, the z -axis is perpendicular to the MCP detector face, and the y -axis is in the plane of the detector and perpendicular to the plane defined by the propagation directions of the laser and molecular beams. In this experimental geometry, it is useful to recognize that when the dissociation laser polarization is along the z -axis, symmetry dictates that the images created by ionization laser polarizations along y and x are simple rotations of each other by 90° . In this case, we can simplify the above expression,

$$I_{\text{iso}}^z = 2\langle N_y^z \rangle + \langle N_z^z \rangle = \sum_i c_i^z \langle B_{\text{iso}}^z(v_i) \rangle, \quad (\text{A14})$$

where the brackets $\langle \rangle$ again indicate a sum over the intensities of each pixel in the image. The constants c_i^F will be used in the fit to the rank 2 parameters.

The next step is to create the anisotropic basis functions,

$$B_{\text{aniso}}^F[\beta, a_q^{(k)}(p)] = B_z^F[\beta, a_q^{(k)}(p)] - B_y^F[\beta, a_q^{(k)}(p)], \quad (\text{A15})$$

for each $a_q^{(k)}(p)$ with the expression for $B_{x,y,z}^F[\beta, a_q^{(k)}(p)]$ given in Eq. (A17). These basis functions are identical in shape to the ones shown by Bracker *et al.*,¹⁷ but differ in their normalization. Yet the dependence of the basis functions on β is inconvenient because, unlike the case for diatomics where β must be either -1 or 2 in the axial recoil limit, for triatomics, β is not generally known *a priori*. In principle, it could be possible to perform some kind of iteration during the fit, but a more simple method is to make the following redefinitions:

$$\begin{aligned} b_0^{(2)}(\parallel) &\equiv (1 + \beta) a_0^{(2)}(\parallel), \\ b_0^{(2)}(\perp) &\equiv (1 - \beta/2) a_0^{(2)}(\perp), \\ b_1^{(2)}(\parallel, \perp) &\equiv \text{Re}[a_1^{(2)}(\parallel, \perp)], \\ b_2^{(2)}(\perp) &\equiv (1 - \beta/2) a_2^{(2)}(\perp). \end{aligned} \quad (\text{A16})$$

One can then use these new $b_q^{(k)}$ parameters in fitting the anisotropic subtraction images I_{aniso}^F . After determining β , we calculate the $a_q^{(k)}(p)$ from the $b_q^{(k)}(p)$ by dividing by the appropriate β factor. The new expressions are

$$B_{x,y,z}^F[b_q^{(k)}(p)] = I(v_i) s_2 \{ b_0^{(2)}(\parallel) \cos^2 \theta_\epsilon P_2(\cos \theta_\epsilon) \\ + b_0^{(2)}(\perp) \sin^2 \theta_\epsilon P_2(\cos \theta_\epsilon) + b_1^{(2)} \\ \times (\parallel, \perp) \sqrt{3/2} \sin \theta_\epsilon \cos \theta_\epsilon \sin 2\Theta \cos \Phi \\ + b_2^{(2)}(\perp) \sqrt{3/2} \sin^2 \theta_\epsilon \sin^2 \Theta \cos 2\Phi \}, \quad (\text{A17})$$

and

$$B_{\text{anisol}}^F[b_q^{(k)}(p)] = B_z^F[b_q^{(k)}(p)] - B_y^F[b_q^{(k)}(p)]. \quad (\text{A18})$$

Thus, we perform the following fit to determine the $b_q^{(k)}$:

$$I_{\text{anisol}}^F = s_2 \sum_{i,q,p} c_i^F b_q^{(2)}(p) B_{\text{anisol}}^F[b_q^{(k)}(p); v_i]. \quad (\text{A19})$$

The quantity (I_{\parallel}/I_{\perp}) contained within the I_{anisol}^F can be measured while taking data, but subtle changes in laser overlap and intensity can produce misleading results. Another approach is to allow I_{\parallel}/I_{\perp} to be determined in the fitting procedure. Once the rank 2 parameters are found, we fit to β_i in the following expression:

$$N_{y,z}^F = \sum_i c_{y,z}^F(i) \left\{ I(v_i) + I(v_i) \beta_i P_2^F(\cos \theta) + s_2 \left[\sum_{q,p} a_q^{(2)}(p) \mathbf{B}_{y,z}^F[a_q^{(2)}(p); v_i] \right] \right\}, \quad (\text{A20})$$

where the $b_q^{(2)}(p)$ and c_i^F are fixed from the previous fit. As mentioned before, the $a_q^{(2)}(p)$ are then calculated from the fitted $b_q^{(2)}(p)$ and β_i values.

5. Density matrix

The angular momentum density matrix is easily calculated from the spherical tensor coefficients. The probability of measuring an angular momentum fragment j with projection m_j is given by^{17,18}

$$\rho_{m'm} = \sum_{k,q} (-1)^{J+q-m'} \frac{(2K+1)[J(J+1)]^{k/2}}{c(k) \langle J \| J^{(k)} \| J \rangle} \times \begin{pmatrix} J & k & J \\ -m & q & m' \end{pmatrix} A_q^{(k)} \quad (\text{A21})$$

for the notation used by the Zare *et al.* $A_q^{(k)}$ are the multiple moments in the molecular frame which contain the second rank alignment parameters. The fractional m_j populations are easily found by properly normalizing the result,

$$P(m) = \frac{\sigma(m;j)}{\sum_m \sigma(m;j)}. \quad (\text{A22})$$

¹C. E. Fairchild, E. J. Stone, and G. M. Lawrence, *J. Chem. Phys.* **69**, 3632 (1978).

²R. K. Sparks, L. R. Carlson, K. Shobatake, M. L. Kowalczyk, and Y. T. Lee, *J. Chem. Phys.* **72**, 1401 (1980).

³D. Stranges, X. Yang, J. D. Chesko, and A. G. Suits, *J. Chem. Phys.* **102**, 6067 (1995).

⁴K. Takahashi, N. Taniguchi, Y. Matsumi, and M. Kawasaki, *Chem. Phys.* **231**, 171 (1998).

⁵M.-A. Thelen, T. Gejo, J. A. Harrison, and J. R. Huber, *J. Chem. Phys.* **103**, 7946 (1995).

⁶J. M. Valentini, D. P. Gerrity, D. L. Phillips, J.-C. Nieh, and K. D. Tabor, *J. Chem. Phys.* **86**, 6745 (1987).

⁷J. J. Valentini, *Chem. Phys. Lett.* **96**, 397 (1983).

⁸A. G. Suits, R. L. Miller, L. S. Bontuyan, and P. L. Houston, *J. Chem. Soc., Faraday Trans. 2* **89**, 1443 (1993).

⁹A. Banichevich, S. D. Peyerimhoff, and F. Grein, *Chem. Phys.* **178**, 155 (1993).

¹⁰C. Leforestier, F. LeQuere, K. Yamashita, and K. Morokuma, *J. Chem. Phys.* **101**, 3806 (1994).

¹¹B. R. Johnson and J. L. Kinsey, *J. Chem. Phys.* **91**, 7638 (1989).

¹²B. R. Johnson and J. L. Kinsey, *Phys. Rev. Lett.* **62**, 1607 (1989).

¹³A. J. Orr-Ewing and R. N. Zare, *Annu. Rev. Phys. Chem.* **45**, 315 (1994).

¹⁴Y. Mo and T. Suzuki, *J. Chem. Phys.* **108**, 6780 (1998).

¹⁵Y. Mo, H. Katayanagi, M. C. Heaven, and T. Suzuki, *Phys. Rev. Lett.* **77**, 830 (1996).

¹⁶L. D. A. Siebbeles, M. Glass-Maujean, O. S. Vasyutinskii, J. A. Beswick, and O. Roncero, *J. Chem. Phys.* **100**, 3610 (1994).

¹⁷A. S. Bracker, E. R. Wouters, A. G. Suits, and O. S. Vasyutinskii, *J. Chem. Phys.* **110**, 6749 (1999).

¹⁸T. P. Rakitzis and R. N. Zare, *J. Chem. Phys.* **110**, 3341 (1999).

¹⁹T. P. Rakitzis, G. E. Hall, M. L. Costen, and R. N. Zare, *J. Chem. Phys.* **111**, 8751 (1999).

²⁰T. P. Rakitzis, S. A. Kandel, A. J. Alexander, and Z. H. Kim, *Science* **281**, 1346 (1998).

²¹Y. Mo and T. Suzuki, *J. Chem. Phys.* **112**, 3463 (2000).

²²Y. Mo and T. Suzuki, *J. Chem. Phys.* **109**, 4691 (1998).

²³A. S. Bracker, E. R. Wouters, A. G. Suits, Y. T. Lee, and O. S. Vasyutinskii, *Phys. Rev. Lett.* **80**, 1626 (1998).

²⁴V. P. Hradil, T. Suzuki, S. A. Hewitt, P. L. Houston, and B. J. Whitaker, *J. Chem. Phys.* **99**, 4455 (1993).

²⁵T. Suzuki, H. Katayanagi, Y. Mo, and K. Tonokura, *Chem. Phys. Lett.* **256**, 90 (1996).

²⁶D. W. Neyer, A. J. R. Heck, D. W. Chandler, J. M. Teule, and M. H. M. Janssen, *J. Phys. Chem. A* **103**, 10388 (1999).

²⁷T. P. Rakitzis, S. A. Kandel, A. J. Alexander, Z. H. Kim, and R. N. Zare, *J. Chem. Phys.* **110**, 3351 (1999).

²⁸M. Ahmed, D. S. Peterka, A. S. Bracker, O. S. Vasyutinskii, and A. G. Suits, *J. Chem. Phys.* **110**, 4115 (1999).

²⁹M. Ahmed, E. R. Wouters, D. S. Peterka, O. S. Vasyutinskii, and A. G. Suits, *Faraday Discuss.* **113**, 425 (1999).

³⁰Z. H. Kim, A. J. Alexander, and R. N. Zare, *J. Phys. Chem. A* **103**, 10144 (1999).

³¹P. L. Houston, *J. Phys. Chem.* **100**, 12757 (1996).

³²B.-Y. Chang, R. C. Hoetzlein, J. A. Mueller, J. D. Geiser, and P. L. Houston, *Rev. Sci. Instrum.* **69**, 1665 (1998).

³³A. T. J. B. Eppink and D. H. Parker, *Rev. Sci. Instrum.* **68**, 3477 (1997).

³⁴S. T. Pratt, P. M. Dehmer, and J. L. Dehmer, *Phys. Rev. A* **43**, 4702 (1991).

³⁵S. T. Pratt, P. M. Dehmer, and J. L. Dehmer, *Phys. Rev. A* **43**, 282 (1991).

³⁶D. J. Bamford, L. E. Jusinski, and W. K. Bischel, *Phys. Rev. A* **34**, 185 (1986).

³⁷D. J. Bamford, M. J. Dyer, and W. K. Bischel, *Phys. Rev. A* **36**, 3497 (1987).

³⁸L. A. Shepp and B. F. Logan, *IEEE Trans. Nucl. Sci.* **ns-21**, 228 (1974).

³⁹L. M. Smith, D. R. Keefer, and S. I. Sudharsanan, *J. Quant. Spectrosc. Radiat. Transf.* **39**, 367 (1988).

⁴⁰M. Kalal and K. A. Nugent, *Appl. Opt.* **27**, 1956 (1988).

⁴¹A. S. Bracker, Ph.D. thesis, University of California at Berkeley, 1997.

⁴²A. C. Kummel, G. O. Sitz, and R. N. Zare, *J. Chem. Phys.* **85**, 6874 (1986).

⁴³N. Taniguchi, K. Takahashi, Y. Matsumi, S. M. Dylewski, J. D. Geiser, and P. L. Houston, *J. Chem. Phys.* **111**, 6350 (1999).

⁴⁴P. J. Hay, R. T. Pack, R. B. Walker, and E. J. Heller, *J. Phys. Chem.* **86**, 862 (1982).

⁴⁵C. Leforestier and R. E. Wyatt, *J. Chem. Phys.* **82**, 752 (1985).

⁴⁶J. D. Geiser, S. M. Dylewski, J. A. Mueller, R. J. Wilson, R. Toumi, and P. L. Houston, *J. Chem. Phys.* **112**, 1279 (2000).

⁴⁷N. Balakrishnan and G. D. Billing, *J. Chem. Phys.* **101**, 2968 (1994).

⁴⁸T. Suzuki, H. Katayanagi, S. Nanbu, and M. Aoyagi, *J. Chem. Phys.* **109**, 5778 (1998).

⁴⁹N. Sivakumar, G. E. Hall, and P. L. Houston, *J. Chem. Phys.* **88**, 3692 (1988).